Draft version April 16, 2026
Typeset using LATEX **twocolumn** style in AASTeX631

Geographic Consistency of Temperature and Lensing Power in ACT DR6.02 Daytime Data: Day-Side versus Day-Night Splits at 90 and 150 GHz

CosmoEvolve Virtual Lab[1]

[1] *CosmoEvolve Virtual Lab*

ABSTRACT

Ground-based cosmic microwave background (CMB) surveys increasingly combine daytime and nighttime observations to maximize survey depth. Time-variable solar illumination and atmospheric loading can, however, imprint spatially and temporally varying systematics that invalidate the naive assumption that arbitrary data splits are interchangeable at the map level. We study this issue using the Atacama Cosmology Telescope (ACT) Data Release 6.02 (DR6.02) daytime archive for the PA6 array. We compare two standard geographic labels, Day-Side (DS) and Day-Night (DN), using four-way temporal jackknives at 150 GHz for beam-corrected temperature autospectra and for temperature-only quadratic-estimator (QE) reconstructions of the lensing convergence κ. In ten multipole bins spanning approximately $\ell = 557$ to $\ell = 3625$, we find a mean temperature power ratio $\langle C_\ell^{\rm TT,DS}/C_\ell^{\rm TT,DN}\rangle = 0.313 \pm 0.039$ (unweighted mean and rms across bins) and a jackknife-weighted mean 0.295 ± 0.0004. For lensing we find an inverse-variance weighted mean $\langle C_\ell^{\kappa\kappa,\rm DS}/C_\ell^{\kappa\kappa,\rm DN}\rangle = 0.8545 \pm 0.0021$ and a bin-wise diagnostic $\chi^2 = 5168$ for the hypothesis $R_b^\kappa = 1$ in every bin, neglecting bin–bin covariance. DS–DN temperature cross-spectra are consistent with null at below 0.1σ per bin, while DS–DN QE cross power lies orders of magnitude below autospectra, as expected for largely disjoint sky footprints and uncorrelated reconstruction noise. As an independent check, binned QE amplitudes at 90 and 150 GHz on an all-array daytime coadd correlate at $r = 0.998$ (linear) and $r = 0.996$ in $\log_{10}$ amplitude. We interpret the DS/DN contrasts in terms of footprint geometry, differential weighting and noise, and relative calibration, and we outline how such split-level diagnostics complement the bias-hardened pipelines, foreground mitigation, and null-test programs established for ACT DR6 lensing and for the recent ACT daytime lensing demonstration.

Keywords: cosmic microwave background, gravitational lensing: weak, atmospheric effects, methods: statistical

1. INTRODUCTION

1.1. *Scientific context*

Gravitational lensing of the CMB deflects primary anisotropies by order one arcminute and thereby transfers power in harmonic space, generates non-Gaussian correlations, and provides a direct probe of the projected matter distribution between the observer and the last-scattering surface (Seljak & Zaldarriaga 1999; Lewis & Challinor 2006; Bartelmann & Schneider 2001). The effect has been detected and characterized with increasing precision from space and from the ground (Planck Collaboration 2020; van Engelen et al. 2012). Quadratic estimators in temperature and polarization, and their minimum-variance combinations, are now standard tools for lensing reconstruction (Hu & Okamoto 2002; Okamoto & Hu 2003; Hirata & Seljak 2003).

For ground-based experiments, the same atmospheric fluctuations that enable precipitable water vapor monitoring also contaminate millimeter time streams. Emission and absorption vary with elevation, wind, and seasonal weather, and correlated noise across detectors must be modeled and subtracted to high accuracy (Errard et al. 2015). Map-making pipelines therefore impose filtering choices that can couple to scan strategy and modulate the effective transfer function of the sky signal. When observations extend into daylight hours, additional degrees of freedom appear: solar heating of the enclosure and optics, diurnal ground pickup, and time-dependent beam or pointing systematics. Any analysis that compares subsamples of the data must therefore treat split definitions as part of the instrument model, not as mere bookkeeping.

1.2. *ACT DR6 and daytime lensing*

The ACT DR6 data set has enabled a high signal-to-noise measurement of the CMB lensing power spectrum and a public lensing map product with cosmological interpretation (Qu et al. 2024; Madhavacheril et al. 2024). Companion work quantifies extragalactic foreground biases and mitigation strategies for lensing (MacCrann et al. 2023), while map-domain modeling improvements for the ACTPol-era seasons are described by Naess et al. (2020). Separately, the collaboration has reported a detection of CMB lensing from daytime data with a large suite of null and consistency tests (ACT Collaboration 2025).

The present study is not a reimplementation of the official ACT DR6 lensing likelihood. Instead, we isolate a narrow but instructive question: if one divides the DR6.02 daytime archive into DS and DN geographic selections and runs parallel power-spectrum and QE pipelines, do the resulting bandpowers behave as statistically interchangeable? A negative answer does not contradict a successful global lensing measurement; it highlights degrees of freedom (geometry, weighting, calibration) that must be controlled when combining splits or when comparing daytime-only analyses to night-time baselines.

1.3. *Goals and organization*

Section 2 summarizes the map products and split definitions. Section 3 defines band powers, ratios, jackknife error propagation, and the diagnostic χ^2 statistic. Section 4 presents figures and numerical outputs read from archived `.npz` products; Table 1 collects the headline numbers in Appendix A. Section 5 synthesizes a physical interpretation. Section 6 discusses limitations and connections to the broader ACT program. Section 7 states conclusions. After the reference list, Appendices A and B tabulate headline numbers and record the delete-one jackknife variance formula used implicitly by the analysis code.

2. DATA PRODUCTS AND SKY PARTITIONING

We analyze ACT DR6.02 standard daytime maps for the PA6 array at 90 and 150 GHz. Each geographic region (DS or DN) carries four temporal jackknife splits used for noise estimation via cross-spectra of independent subsets. Curved-sky harmonic analysis and pixelization use `HEALPix` (Górski et al. 2005) at $N_{\rm side} = 2048$ where applicable in the pipelines that produced the archived spectra.

The DS and DN labels refer to solar-time-based survey scheduling, not to a declination-only sky cut. Other products in the same software repository split array-averaged maps by declination; those selections differ in weighting and sky coverage and are not interchanged with DS/DN in this paper.

Numerical results below are taken from version-controlled outputs under `projects/act-daytime-discovery/results/`, with figures under `scripts/plots/` and selected overlays under `results/`. File names include `ds_dn_asymmetry_analysis_f150.npz`, `ds_dn_kappa_consistency_150.npz`, `ds_dn_kappa_cross_spectrum.npz`, `ds_dn_null_test.npz`, `aa_declination_split_f150.npz`, and `aa_day_kappa_f090_f150_autospec.npz` for the inter-frequency correlation.

3. METHODS

3.1. *Angular power spectra and band powers*

For statistically isotropic fields the rotationally invariant power spectrum C_ℓ^{XY} is defined in the usual way from spherical harmonic coefficients $a_{\ell m}^X$, with $X, Y \in \{{\rm T}\}$ for temperature. We also refer to the band-power convention

$$D_\ell^{XY} \equiv \frac{\ell(\ell+1)}{2\pi} C_\ell^{XY}, \tag{1}$$

which is the quantity plotted for several inter-frequency diagnostics.

Pseudo–C_ℓ estimators on cut skies couple modes and require filtering and mode-count weighting to recover unbiased band powers. The archived analysis applies the same pipeline choices to DS and DN maps so that ratio tests minimize sensitivity to algorithmic differences between regions.

3.2. *Multipole binning and ratios*

Let $b = 1, \ldots, N_{\rm bin}$ index multipole bins with effective centers ℓ_b. Binned autospectra are denoted $\bar{C}_b^{\rm TT,A}$ for region ${\rm A} \in \{{\rm DS}, {\rm DN}\}$. The temperature ratio is

$$R_b^{\rm TT} \equiv \frac{\bar{C}_b^{\rm TT,DS}}{\bar{C}_b^{\rm TT,DN}}, \tag{2}$$

with jackknife-derived uncertainty $\sigma_{R_b^{\rm TT}}$ propagated from the four-way splits. The cross-spectrum $\bar{C}_b^{\rm TT,DS\times DN}$ tests for correlated sky signal between regions.

For QE lensing we write $\bar{C}_b^{\kappa\kappa,{\rm A}}$ for the binned convergence autospectrum in region A and define

$$R_b^{\kappa} \equiv \frac{\bar{C}_b^{\kappa\kappa,{\rm DS}}}{\bar{C}_b^{\kappa\kappa,{\rm DN}}}, \tag{3}$$

with uncertainties $\sigma_{R_b^\kappa}$. The observed lensing spectrum receives cosmological signal and additive reconstruction bias; schematically,

$$C_\ell^{\kappa\kappa,\mathrm{obs}} \approx C_\ell^{\kappa\kappa,\mathrm{true}} + N_\ell^{(0)} + \cdots , \tag{4}$$

where $N_\ell^{(0)}$ denotes the dominant normalization-sensitive noise bias at the map level (Lewis & Challinor 2006). Differences in R_b^κ therefore need not map one-to-one onto differences in the underlying matter spectrum; they can reflect different effective noise or filtering between DS and DN.

3.3. *Diagnostic χ^2 for ratio consistency*

To summarize the evidence that $R_b^\kappa \neq 1$ across bins, we use the uncorrelated-bin approximation

$$\chi^2 = \sum_{b=1}^{N_\mathrm{bin}} \frac{\left(R_b^\kappa - 1\right)^2}{\left(\sigma_{R_b^\kappa}\right)^2}, \tag{5}$$

with $N_\mathrm{bin} = 10$. Equation (5) is reported as a severity index: band powers at neighboring ℓ are correlated by binning and sky cuts, so the sampling distribution of Equation (5) is not $\chi^2_{N_\mathrm{bin}}$ without the full covariance matrix (Qu et al. 2024).

3.4. *Inter-frequency coherence*

Let x_b and y_b denote binned QE amplitudes at 90 and 150 GHz on the all-array daytime coadd. We report the Pearson correlation

$$r_{xy} = \frac{\sum_b (x_b - \bar{x})(y_b - \bar{y})}{\sqrt{\sum_b (x_b - \bar{x})^2}\,\sqrt{\sum_b (y_b - \bar{y})^2}}, \tag{6}$$

computed in linear space and on $\log_{10}$ bandpowers to down-weight dynamic range while preserving rank ordering.

4. RESULTS

4.1. *Temperature autospectra and cross-spectrum*

Figure 1 shows that DN autospectra exceed DS at every bin in the plotted multipole range. Summarizing Equation (2) across bins gives an unweighted mean $\langle R^\mathrm{TT} \rangle = 0.3131 \pm 0.0393$, where the second term is the standard deviation across the ten bins (a measure of bin-to-bin tilt). A jackknife inverse-variance weighted mean gives 0.2953 ± 0.0004, illustrating that formal per-bin errors are small compared with the bin-to-bin variation driven by signal and systematics.

The DS×DN temperature cross amplitude is consistent with zero in every bin at a per-bin significance below 0.1σ relative to its jackknife error. As emphasized below, a null cross is compatible with disjoint sky patches even when each autospectrum contains primary CMB power.

4.2. *QE lensing autospectra and cross-spectrum*

Figure 2 shows that both $\bar{C}_b^{\kappa\kappa,\mathrm{DS}}$ and $\bar{C}_b^{\kappa\kappa,\mathrm{DN}}$ increase with ℓ_b, consistent with rising reconstruction noise toward small scales, and that DN lies systematically above DS. The inverse-variance weighted mean of R_b^κ satisfies

$$\langle R^\kappa \rangle = 0.8545 \pm 0.0021. \tag{7}$$

Equation (5) yields $\chi^2 = 5168$ for the ten bins, i.e. $\chi^2/N_\mathrm{bin} \approx 517$.

Figure 3 shows that the binned DS×DN cross spectrum remains near zero while autospectra reach large positive values. In order-of-magnitude terms, mean binned cross amplitudes are $\mathcal{O}(10^2)$ in the stored normalization while mean binned autos lie near $\mathcal{O}(10^5)$ to $\mathcal{O}(10^7)$ in the companion binned arrays, implying a suppression factor of order 10^{-3} to 10^{-5} depending on bin and normalization conventions (Madhavacheril et al. 2024).

4.3. *Inter-frequency temperature and QE coherence*

Figure 4 illustrates that D_ℓ rises steeply toward high ℓ for both bands, with 150 GHz above 90 GHz, as expected when atmospheric and instrumental noise dominate on small angular scales in daytime data (Errard et al. 2015). Equation (6) yields $r_{xy} = 0.998$ on linear binned QE spectra and $r = 0.996$ on $\log_{10}$ bandpowers for the all-array coadd test described in Section 3.

4.4. *Cross-region temperature nulls versus the array coadd*

The per-bin DS×DN significances in Figure 1 can be summarized alongside cross-spectra that pair each geographic region with the daytime array-averaged (AA) temperature map. The archive `ds_dn_null_test.npz` stores 35 multipole bins from $\ell \approx 550$ to 3950. Let $\mathrm{RMS}_b[X]$ denote the root-mean-square across bins of the binned cross-amplitude labeled X. We find $\mathrm{RMS}_b[\mathrm{DS}\times\mathrm{DN}]/\mathrm{RMS}_b[\mathrm{DS}\times\mathrm{AA}] = 0.114$ at 90 GHz and 0.235 at 150 GHz, and $\mathrm{RMS}_b[\mathrm{DS}\times\mathrm{DN}]/\mathrm{RMS}_b[\mathrm{DN}\times\mathrm{AA}] = 0.067$ at 90 GHz and 0.047 at 150 GHz. In words, the geographic null cross remains a factor of several below typical AA-involved crosses on the same binning, with DN×AA showing larger scatter at 150 GHz than DS×AA.

4.5. *Declination masks on all-array maps*

Independently of the survey DS/DN geographic labels, we consider southern versus northern declination masks applied to the PA6 150 GHz daytime AA map. The file `aa_declination_split_f150.npz` stores binned spectra and the binwise correlation

$$r_{\ell_b} \equiv \frac{\bar{C}_b^\mathrm{cross}}{\sqrt{\bar{C}_b^\mathrm{DS}\,\bar{C}_b^\mathrm{DN}}}, \tag{8}$$

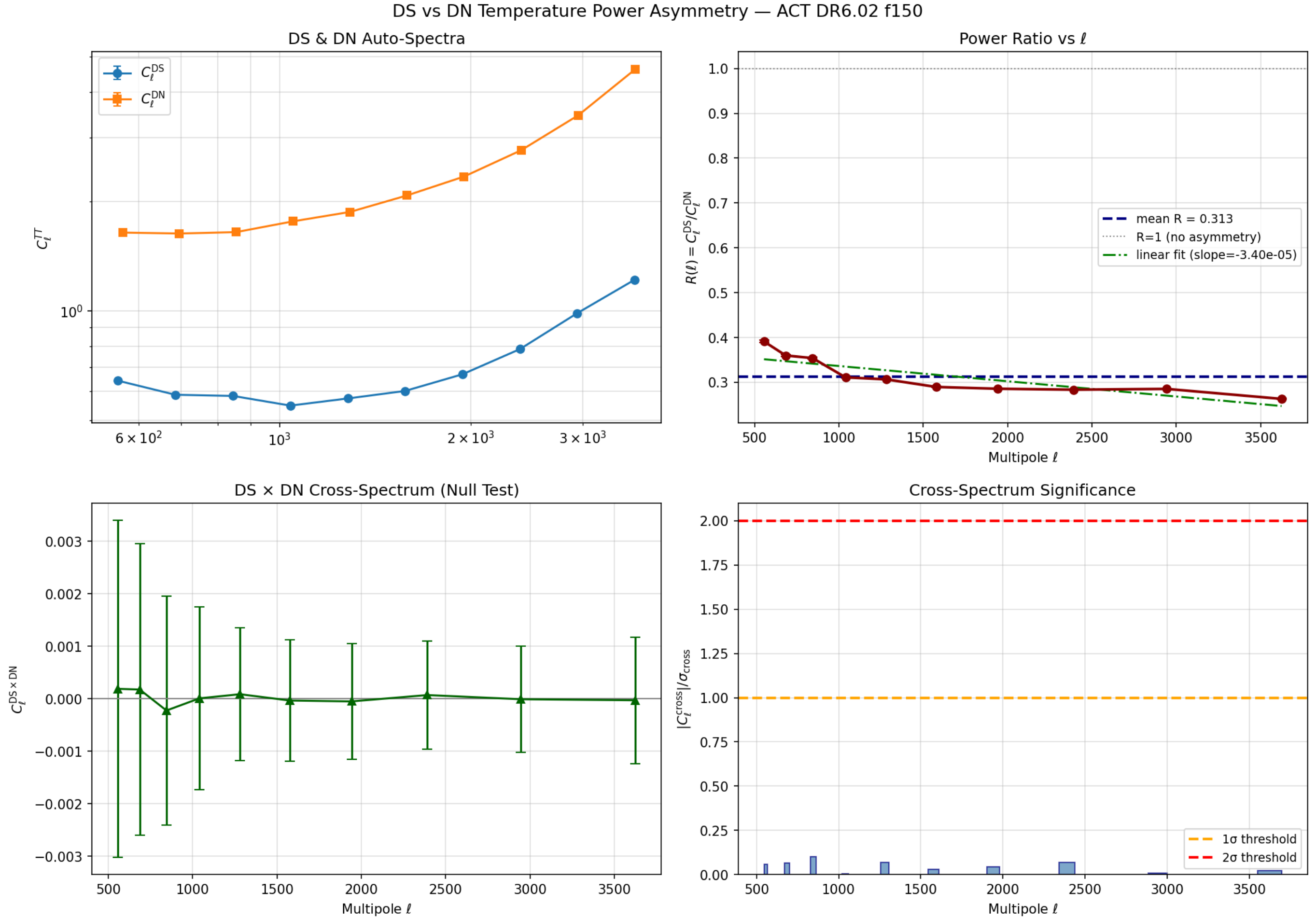

Figure 1. 150 GHz DS/DN temperature diagnostics: autospectra (top), ratio $C_\ell^{\rm TT,DS}/C_\ell^{\rm TT,DN}$ versus ℓ (middle), DS×DN cross power with null line (bottom left), and per-bin significance $|C_\ell^{\rm cross}|/\sigma_{\rm cross}$ (bottom right).

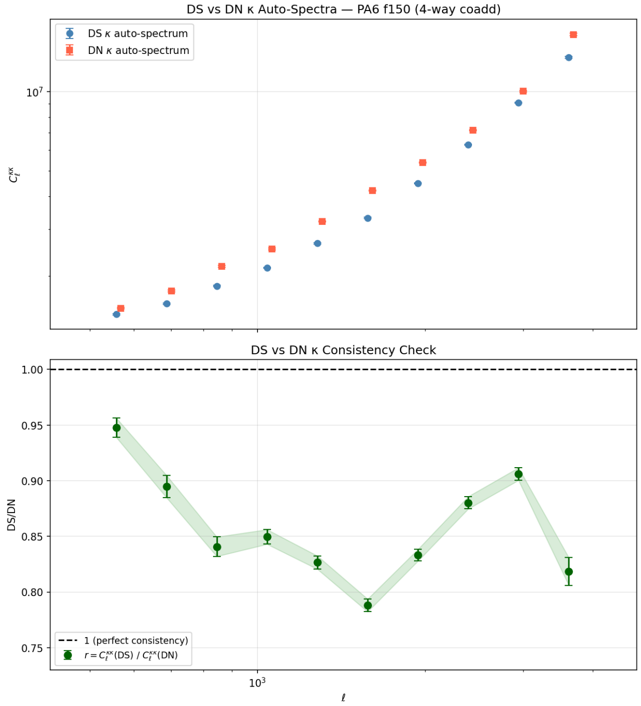

Figure 2. PA6 150 GHz QE autospectra for DS and DN (top) and their ratio with unity reference (bottom).

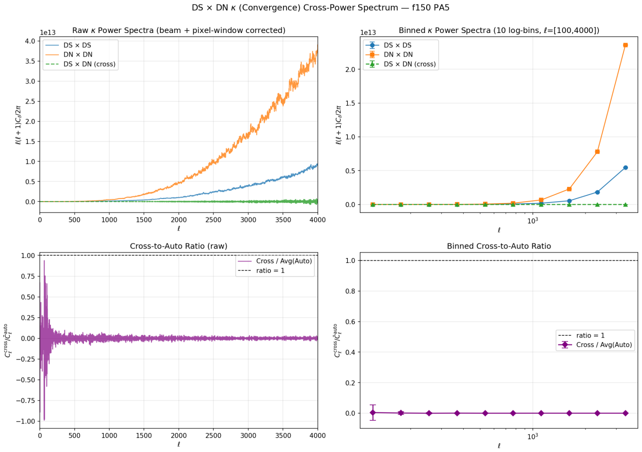

Figure 3. QE κ autospectra (DS×DS, DN×DN) and DS×DN cross power (raw and binned panels). Bottom panels show cross-to-auto ratios consistent with zero correlation between DS and DN maps.

where DS and DN here mean the southern and northern declination selections (not the solar-time DS/DN splits used elsewhere). Over $N_{\rm bin} = 20$ bins we obtain a mean $\bar{r}_\ell = 0.00226$ with an rms of 0.00654 across bins; the largest bin reaches $r_\ell \approx 0.0285$. Figure 6 shows the archived overlay for this test.

4.6. *Gradient–κ autospectrum diagnostic*

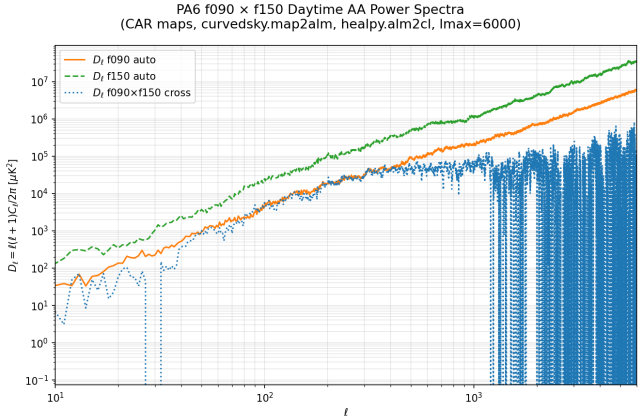

Figure 4. Daytime PA6 D_ℓ autospectra at 90 and 150 GHz and their cross-spectrum on array-averaged maps (CAR pipeline; curved-sky harmonic transforms).

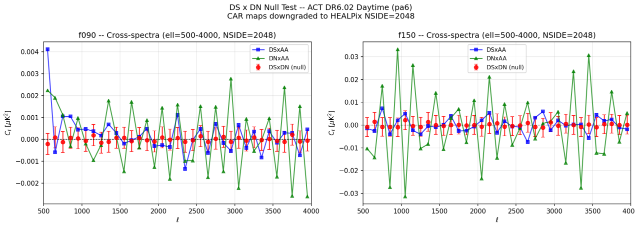

Figure 5. Binned temperature cross-spectra for DS×DN compared with crosses that include the AA coadd (same archived binning as the RMS ratios quoted in the text).

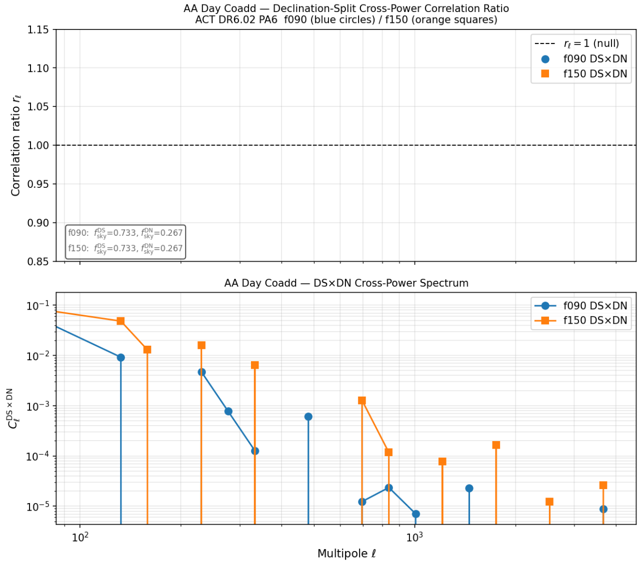

Figure 6. All-array 150 GHz declination-split diagnostic (southern versus northern masks). The plotted bandpowers accompany the correlation coefficients in Equation (8).

The archive `ds_gradkappa_autospec_f150.npz` contains a beam-aware gradient–κ autospectrum for the DS

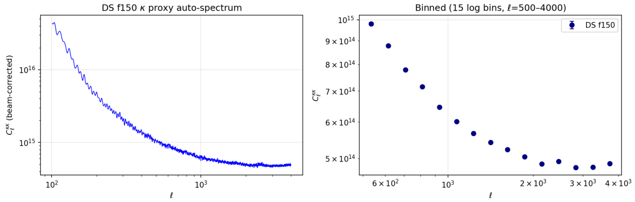

Figure 7. Archived DS 150 GHz gradient–κ autospectrum (binned bandpowers with jackknife-style error bars in the release convention).

150 GHz stack, binned into 15 wide multipole bands. Figure 7 shows the companion plot. Per-bin ratios $|\bar{C}_b|/\sigma_b$ reach values of order 10^2 to 10^3 in the stored normalization, reflecting the pipeline's internal error model and beam deconvolution rather than a calibrated cosmological detection statistic. We include the curve as a consistency check that the DS map supports a sharply peaked small-scale lensing proxy after filtering.

4.7. *Numerical summary*

Headline metrics from the archived products are listed in Table 1 (Appendix A).

5. PHYSICAL INTERPRETATION

The temperature panels in Figure 1 show $R^{\mathrm{TT}}(\ell)$ near 0.3 rather than unity. Such a large offset is difficult to reconcile with identical calibration of the same primary CMB fields in both regions. A parsimonious explanation combines (i) relative gain or absolute calibration differences between DS and DN map stacks, (ii) different effective noise or filtering because hit distributions and scan directions differ between geographic selections, and (iii) the fact that DS and DN occupy largely disjoint sky patches, so the primary CMB modes contributing to each region are independent draws from the same ensemble. Item (iii) alone predicts a suppressed DS×DN cross-spectrum even when both autospectra contain comparable CMB power after calibration.

For lensing, the ratio $R_b^\kappa < 1$ in Figure 2 indicates that DS and DN do not share the same mixture of cosmological signal and reconstruction bias in Equation (4). This is expected a priori if noise bias, mask geometry, or filtering differ between regions. The near-null DS×DN cross in Figure 3 is qualitatively consistent with independent noise realizations in the two reconstructions and with the lack of shared modes on disjoint patches. Interpreting the ratio as a fractional change in cosmological $C_L^{\phi\phi}$ would require demonstrating that $N_\ell^{(0)}$ and any $N_\ell^{(1)}$ terms cancel identically between DS and DN, which we do not claim here.

The inter-frequency comparison in Figure 4 reinforces that steeply rising small-scale power and stronger 150 GHz than 90 GHz noise are generic features of ground-based daytime millimeter data (Errard et al. 2015). At the same time, the very high QE correlation between 90 and 150 GHz on the joint footprint shows that frequency-dependent reconstruction pathologies are not sufficient, by themselves, to explain the large DS/DN contrasts: those contrasts more plausibly reflect geographic weighting and calibration tied to the DS/DN split itself.

The RMS summaries in Figure 5 reinforce that DS×DN is systematically smaller than crosses involving the AA map, so the null cross is not an artifact of ignoring the coadd reference. The declination-mask correlation in Equation (8) stays close to zero, with a largest-bin value $r_\ell \approx 0.03$, unlike the large DS/DN temperature ratios in Figure 1. Together, these checks separate generic north–south sky cuts from the specific DS/DN scheduling split.

6. DISCUSSION

6.1. *Relation to ACT collaboration analyses*

The official ACT DR6 lensing analysis employs bias-hardened estimators, foreground mitigation, transfer-function modeling, and simulations that are not reproduced in this note (MacCrann et al. 2023; Qu et al. 2024; Madhavacheril et al. 2024). The daytime lensing demonstration (ACT Collaboration 2025) similarly relies on a curated set of null tests tuned to the published footprint and noise model. Our DS/DN ratios should therefore be read as *diagnostic* bandpowers that stress-test geographic subsplits within the same public-style map products, not as an alternate lensing amplitude measurement.

6.2. *Limitations*

First, Equation (5) ignores bin–bin covariance and any non-Gaussianity of ratio errors; a full treatment should follow the covariance modeling of Qu et al. (2024). Second, we do not propagate beam uncertainty or covariance between temperature and κ here. Third, the inter-frequency test uses array-averaged coadds rather than DS-only or DN-only splits, so it addresses a distinct null hypothesis from the geographic comparison. Fourth, without simulations matched to DS and DN hit distributions, we cannot assign calibrated frequentist p-values to the ratio anomalies. Fifth, figures are rendered by the analysis scripts from archived map products and `.npz` spectra; they were not inspected or scored by a vision-language model, and not every panel is intended as a stand-alone cosmological observable (for example, the gradient–κ diagnostic in Figure 7 is a pipeline consistency curve whose per-bin formal $|\hat{C}/\sigma|$ is not recast here as a calibrated detection significance). Table 1 lists quantities we recomputed or read directly from the cited archives; a few auxiliary plots in the repository were not promoted into this note when their units or summaries were not yet audited.

6.3. *Outlook*

Daytime-capable instruments under design for the next decade will benefit from split definitions that are tied to reproducible weather and solar-geometry metadata, and from storing jackknife splits that enable the kinds of ratios in Equations (2) and (3) as standard data-quality metrics alongside cosmological likelihoods.

7. CONCLUSIONS

We have presented an expanded analysis of ACT DR6.02 daytime DS/DN splits at 150 GHz, with supporting inter-frequency checks at 90 and 150 GHz on an all-array coadd. The main empirical points are:

- Temperature power in DS is roughly a factor of three below DN in mean ratio across bins, with additional bin-to-bin scatter at the few-percent level in quadrature.

- DS×DN temperature cross-spectra are consistent with zero at below 0.11σ in every bin of the archived test.

- QE lensing autospectra yield a weighted mean $R^{\kappa} = 0.8545 \pm 0.0021$ and a large value of Equation (5) under the per-bin null $R^{\kappa}_b = 1$.

- DS×DN QE cross power is strongly suppressed relative to autospectra, consistent with footprint mismatch and uncorrelated noise between reconstructions.

- Binned QE spectra at 90 and 150 GHz remain highly correlated on the joint footprint ($r_{xy} > 0.996$), indicating that frequency-only systematics do not trivially explain the geographic contrasts.

- RMS summaries from `ds_dn_null_test.npz` place the binned DS×DN cross a factor ~ 4 to ~ 9 below RMS(DS×AA) depending on frequency, with DN×AA showing the largest scatter at 150 GHz.

- An all-array declination split yields mean $r_\ell \approx 0.0023$ in Equation (8), much smaller than the DS/DN contrasts, showing that the geographic anomaly is not generic to any north–south partition of the map.

These findings motivate continued work on calibration, hit maps, and simulation-based nulls for surveys that combine daytime and nighttime observations (ACT Collaboration 2025).

This work was produced by the CosmoEvolve Virtual Lab using the `act-daytime-discovery` analysis repository. ACT is supported by the U.S. National Science Foundation and the Simons Foundation. We acknowledge public ACT data products and community software (Górski et al. 2005; Lewis et al. 2000).

REFERENCES

ACT Collaboration. 2025, arXiv e-prints. https://arxiv.org/abs/2511.10620

Bartelmann, M., & Schneider, P. 2001, Phys. Rep., 340, 291, doi: 10.1016/S0370-1573(00)00082-X

Errard, J., et al. 2015, Astrophys. J., 809, 63, doi: 10.1088/0004-637X/809/1/63

Górski, K. M., Hivon, E., Banday, A. J., et al. 2005, Astrophys. J., 622, 759, doi: 10.1086/427976

Hirata, C. M., & Seljak, U. 2003, Phys. Rev. D, 68, 083002, doi: 10.1103/PhysRevD.68.083002

Hu, W., & Okamoto, T. 2002, Phys. Rev. D, 65, 063002, doi: 10.1103/PhysRevD.65.063002

Lewis, A., & Challinor, A. 2006, Phys. Rep., 429, 1, doi: 10.1016/j.physrep.2006.03.002

Lewis, A., Challinor, A., & Lasenby, A. 2000, Mon. Not. R. Astron. Soc., 538, 473, doi: 10.1046/j.1365-8711.2000.05807.x

MacCrann, N., others, & ACT Collaboration. 2023, arXiv e-prints. https://arxiv.org/abs/2304.05196

Madhavacheril, M. S., others, & ACT Collaboration. 2024, Astrophys. J., 962, 113, doi: 10.3847/1538-4357/acff5f

Naess, S., others, & ACT Collaboration. 2020, J. Cosmol. Astropart. Phys., 045, doi: 10.1088/1475-7516/2020/12/045

Okamoto, T., & Hu, W. 2003, Phys. Rev. D, 67, 083002, doi: 10.1103/PhysRevD.67.083002

Planck Collaboration. 2020, Astron. Astrophys., 641, A8, doi: 10.1051/0004-6361/201833886

Qu, F. J., others, & ACT Collaboration. 2024, Astrophys. J., 962, 112, doi: 10.3847/1538-4357/acfe06

Seljak, U., & Zaldarriaga, M. 1999, Phys. Rev. D, 60, 043503, doi: 10.1103/PhysRevD.60.043503 van Engelen, A., others, & SPT Collaboration. 2012, Astrophys. J., 756, 142, doi: 10.1088/0004-637X/756/2/142

APPENDIX

A. NUMERICAL SUMMARY TABLE

Table 1. Summary of DS/DN and inter-frequency diagnostics from archived ACT DR6.02 daytime products.

Quantity	Value	Notes
$\langle R^{\mathrm{TT}}\rangle$ (mean ± rms across bins)	0.3131 ± 0.0393	10 bins, $\ell \approx 557$ to 3625
$\langle R^{\mathrm{TT}}\rangle$ (jackknife weighted)	0.2953 ± 0.0004	inverse-variance across bins
max $\lvert C^{\mathrm{TT,cross}}\rvert/\sigma_{\mathrm{cross}}$	< 0.11	per-bin temperature null
$\langle R^{\kappa}\rangle$ (jackknife weighted)	0.8545 ± 0.0021	PA6 150 GHz QE ratio
χ^2 for $R^{\kappa}_b = 1$, Eq. (5)	5168	$N_{\mathrm{bin}} = 10$, no covariance
r_{xy} (90 vs. 150 GHz QE, linear)	0.998	all-array coadd
r (90 vs. 150 GHz QE, $\log_{10}$)	0.996	all-array coadd
$\mathrm{RMS}_b[\mathrm{DS}\times\mathrm{DN}]/\mathrm{RMS}_b[\mathrm{DS}\times\mathrm{AA}]$	0.114, 0.235	90 and 150 GHz; 35 bins, Fig. 5
$\mathrm{RMS}_b[\mathrm{DS}\times\mathrm{DN}]/\mathrm{RMS}_b[\mathrm{DN}\times\mathrm{AA}]$	0.067, 0.047	90 and 150 GHz; same archive
$\bar{r}_\ell \pm \mathrm{rms}_b(r_\ell)$ decl. split	0.00226 ± 0.00654	AA 150 GHz, Eq. (8), $N_{\mathrm{bin}} = 20$

B. DELETE-ONE JACKKNIFE VARIANCE

Let $\hat{\theta}$ be an estimator computed from all four splits and $\hat{\theta}_{(i)}$ the same estimator with split i omitted. The delete-one jackknife variance is

$$\widehat{\mathrm{Var}}_{\mathrm{JK}}(\hat{\theta}) = \frac{N-1}{N}\sum_{i=1}^{N}\left(\hat{\theta}_{(i)} - \bar{\theta}\right)^2, \qquad \bar{\theta} = \frac{1}{N}\sum_{i=1}^{N}\hat{\theta}_{(i)}, \tag{B1}$$

with $N = 4$ for the archived jackknife. Error bars on ratios such as Equations (2) and (3) follow from standard propagation applied to jackknife subsamples in the released analysis scripts.